To cite this version :

Bousquet, Yannick and Binder, Nicolas and Dufour, Guillaume and Carbonneau, Xavier and Roumeas, Mathieu and Trébinjac, Isabelle Numerical Simulation of Stall Inception Mechanisms in a Centrifugal Compressor With Vaned Diffuser. (2016) Journal of Turbomachinery, vol. 138 (n° 12). pp. 1-9. ISSN 0889-504X

Y. Bousquet[1]

ISAE,
Université de Toulouse,
10 Avenue Edouard Belin BP 54032,
Cedex 4,
Toulouse 31055, France
e-mail: Yannick.Bousquet@isae.fr

N. Binder

ISAE,
Université de Toulouse,
10 Avenue Edouard Belin BP 54032,
Cedex 4,
Toulouse 31055, France
e-mail: Nicolas.Binder@isae.fr

G. Dufour

ISAE,
Université de Toulouse,
10 Avenue Edouard Belin BP 54032,
Cedex 4,
Toulouse 31055, France
e-mail: Guillaume.Dufour@isae.fr

X. Carbonneau

ISAE,
Université de Toulouse,
10 Avenue Edouard Belin BP 54032,
Cedex 4,
Toulouse 31055, France
e-mail: Xavier.Carbonneau@isae.fr

M. Roumeas

Liebherr-Aerospace Toulouse SAS,
408 Avenue des Etats Unis,
Toulouse 31016, France
e-mail: Mathieu.Roumeas@liebherr.fr

I. Trebinjac

Laboratoire de Mécanique des,
Fluides et d'Acoustique,
UMR CNRS 5509 Ecole Centrale de Lyon,
UCB Lyon 1,
INSA,
36 Avenue Guy de Collongue,
Ecully Cedex 69134, France

Numerical Simulation of Stall Inception Mechanisms in a Centrifugal Compressor With Vaned Diffuser

The present paper numerically investigates the stall inception mechanisms in a centrifugal compressor stage composed of a splittered unshrouded impeller and a vaned diffuser. Unsteady numerical simulations have been conducted on a calculation domain comprising all the blade passages over 360 deg for the impeller and the diffuser. Three stable operating points are simulated along a speed line, and the full path to instability is investigated. The paper focusses first on the effects of the mass flow reduction on the flow topology at the inlet of both components. Then, a detailed analysis of stall inception mechanisms is proposed. It is shown that at the inlet of both components, the mass flow reduction induces boundary layer separation on the blade suction side, which results in a vortex tube having its upper end at the casing and its lower end at the blade wall. Some similarities with flows in axial compressor operating at stall condition are outlined. The stall inception process starts with the growth of the amplitude of a modal wave rotating in the vaneless space. As the flow in the compressor is subsonic, the wave propagates upstream and interacts with the impeller flow structure. This interaction leads to the drop in the impeller pressure ratio. [DOI: 10.1115/1.4033704]

1 Introduction

Centrifugal compressor stages are used in many industrial applications. In the aeronautical domain, the trend has been toward the design of high-speed impeller associated with a vaned diffuser to maximize the efficiency and the pressure ratio, as well as to minimize the size of the stage. Designing a centrifugal compressor stage with a broad operating range constitutes also a new challenge. As for axial configurations, the operating range of the centrifugal compressors is limited at low mass flow rate by the emergence of stall and surge phenomena [1,2]. The operation of the compressor in such modes induces a drop in performance but may also cause mechanical failures. Therefore, a surge margin is usually imposed to prevent the compressor operation in such unstable regimes. As a consequence, the operating range is reduced by the width of the surge margin.

The need to design compressors with broad operating range has prompted many research works. Different flow control strategies are presented by Skoch [3]. Reducing the surge margin is also a way to extend the operating range. However, both solutions require a good comprehension of the mechanisms that may occur before and during the stall onset, in order to detect and control efficiently the emergence of flow instabilities.

In axial compressors, stall inception mechanisms are today well identified. Around 1990 s, McDougall et al. [4] and Day [5] showed two different processes leading to stall. The first one is through the emergence of a modal wave with a small amplitude and a large scale (compressor circumference) called modal stall. The second one is through the growth of a larger amplitude disturbance but with smaller length scale (several blade passages)

named spike. Since then, extensive studies have been carried out to understand the origin of these disturbances. The growth of the modal wave occurs when the compressor operates on the positive slope of the characteristic curve [6]. Considering the spike disturbance, the work of Pullan et al. [7] shows that spike formation originates from flow separation resulting in a vortex formation and propagation around the annulus. A synthetic and objective review of the research about this topic is proposed by Day [8].

The mechanisms leading to stall onset in centrifugal machines are less understood due to the large variety of configurations found in the literature. For example, Trebinjac et al. [9], Spakovszky and Roduner [10], and Toyama et al. [11] focus on high-pressure ratio compressors (above 5) with vaned diffusers. For these configurations, stall occurs in the diffuser entry region. Some other studies [12,13] focus on low-pressure ratio centrifugal compressor (below 2) using vaneless diffuser. For these configurations, rotating stall may occur in the vaneless space or at the impeller inlet. Moreover, these studies are mainly based on experimental procedure through high-frequency pressure measurements. This only allows a partial description of the spatial flow topology before and during the stall inception.

The present work brings a new contribution to the topic by investigating deeply the stall inception mechanism on a moderate (2.5) pressure ratio centrifugal compressor stage with vaned diffuser. The investigations are based on unsteady numerical simulation results including all the blade passages of the impeller and of the diffuser over 360 deg. The test case is composed of a high-speed impeller associated with a vaned diffuser but reaches a moderate pressure ratio (2.5) at the design operating point. There are two main objectives in this paper. The first one is to analyze the evolution of the flow structure when the operating point moves toward low mass flow rate. The second one is to investigate the mechanisms responsible for the stall onset.

Following this Introduction, the test case is described together with the numerical procedure in a first part of the paper. Then, the modifications of the flow structure induced by the mass flow reduction are presented. Finally, the last part of the paper details the mechanisms that are responsible for the stall onset.

2 Test Case Description

The centrifugal compressor test case has been designed by Liebherr-Aerospace Toulouse SAS. It is part of an air-conditioning system. The stage is composed of a backswept splittered unshrouded impeller and a radial vaned diffuser. The specifications are based on a stage total–total pressure ratio of 2.5 at the design rotation speed (38,000 rpm). The impeller is composed of eight main blades and eight splitter blades. The exit radius is around 100 mm. The gap at the tip of the blade changes from the leading edge to the trailing edge. It represents 0.5% of the blade span at the leading edge and 3% at the trailing edge. The vaned diffuser consists of 21 wedge-type blades. Figure 1 shows a three-dimensional view of the stage.
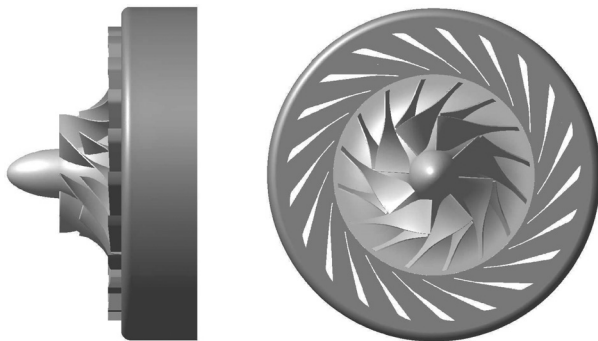
3 Numerical Procedure

3.1 Flow Solver and Physical Model. Simulations are performed with the ELSA software developed by ONERA and CERFACS. More information about the code can be found in Ref. [14]. It is based on a cell-centered approach on multiblock structured grids. The code solves the unsteady compressible Navier–Stokes equations. Turbulence is modeled according to the Reynolds decomposition, and the equations are closed using the single-equation Spalart–Allmaras turbulence model [15]. The convective fluxes are computed with a centered second-order scheme with artificial dissipation of Jameson type and the diffusive fluxes with a second-order centered scheme. Time integration relies on the implicit second-order Gear scheme, coupled with the dual time-stepping method proposed by Jameson [16]. The time-marching in the inner loop is performed with an implicit scheme composed of the backward Euler scheme and a scalar lower–upper symmetric successive over-relaxation method [17]. The number of physical time steps to discretize a complete rotation is set to 1680, corresponding to 210 time steps per impeller main blade passing period and 80 time steps per diffuser blade passing period. The value of the time step is set according to previous work, which aims to study its influence on the flow topology. Then, the value retained permits to obtain time-step independent results. For each physical time step, subiterations are performed in the inner loop until a reduction of 2 orders of magnitude is reached for the residuals. This condition is generally reached in less than ten subiterations.

3.2 Mesh Parameters. The numerical domain is discretized with a structured mesh generated with Autogrid V5 (Numeca, Belgium), using classical H, O, and C topologies for the impeller and the diffuser blade passages. The number of points in each direction of the different blocks is set according to a previous study [18] realized on the same configuration. The size of the first cell is set to 3 μm corresponding to a normalized wall distance y^+ below 3 at the walls. The impeller main blade passage grid and splitter blade passage grid consist of 89 points in the spanwise direction including 29 points in the gap region, 92 points in the pitchwise direction, and 161 points in the streamwise direction. The diffuser blade passage contains 57 points in the spanwise direction, 119 points in the pitchwise direction, and 141 points in the streamwise direction. The impeller blade passage and the diffuser blade passage include 2.6×10^6 and 1.7×10^6 grid cells, respectively. The single passage of each row is repeated to obtain the full annulus. Finally, the calculation domain reaches a total of approximately 60×10^6 points. Figure 2 represents a meridional view of the computational domain.

3.3 Boundary Conditions. At the inlet of the domain, the absolute total pressure, the absolute total temperature, the flow angles (axial flow), and the turbulent intensity are prescribed. The
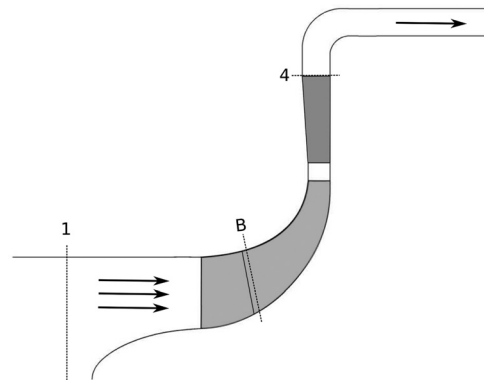

Fig. 1 Three-dimensional sketch of the compressor stage

Fig. 2 Meridional view of the compressor stage

rotor–stator interface is treated with a sliding mesh method [19] that uses a distribution of fluxes. This approach is rigorously conservative for planar interfaces. The blades, hub, and shroud walls are treated with no-slip adiabatic conditions. Considering the outlet boundary condition, experimental data have shown that the characteristic curve of the compressor stage has a positive slope at low mass flow rate. Therefore, the simulation of near stall operating point is not possible with an outlet pressure condition. A mass flow condition is also not adapted due to expected large mass flow evolution during the stall transient. Therefore, the outlet is modeled using a throttle condition, coupled with a simplified radial equilibrium law. The outlet static pressure imposed p_{s5} is set at each time step according to the following equation:

$$p_{s5}(n+1) = p_{t0} + \lambda \dot{m}(n)^2 \qquad (1)$$

where P_{t0} is the inlet total pressure, $\dot{m}(n)$ is the mass flow rate at the iteration n through the exit section, and λ is the throttle parameter. This boundary condition permits to describe the characteristic curves of the compressor from choke to stall by simply increasing the throttle parameter value. This boundary condition is the most appropriate to simulate the stall transient as the pressure imposed is a function of the mass flow rate.

According to one-dimensional stability theory of a compression system [1], the loss of stability can occur in a static mode or in a dynamic mode. Stability criteria for both types of instability can be found in the literature (see, for example, Ref. [2]). The static instability occurs when the slope of the compressor characteristic is higher than the one of the throttle. The occurrence of dynamic instability depends on compressor system characteristics, such as the size of the upstream and downstream volume, the length, and the area of the duct. The numerical domain does not contain any significant volume. Then, the loss of stability of the compressor is a static type. It is then the slope of the throttle characteristic that determines the point of instability.

3.4 Computational Time and Data Extraction. At least 12 physical impeller rotations are needed to reach the periodic state. This is equivalent to approximately 20,000 physical time steps. Simulations are performed by using 512 computing cores and require approximately 200,000 central processing unit hours for a single operating point. Unsteady simulations have been performed to simulate three stable operating points and the stall transient. The three stable operating points are referenced as OP1 (peak efficiency), OP2 (near the maximum pressure ratio), and OP3 (operating point on the positive slope of the compressor characteristic). The objectives of the simulations of the three operating points are to analyze the evolution of the flow topology induced by the mass flow reduction. As will be detailed later, flow unsteadiness for the OP1 and OP2 is only generated by impeller–diffuser interactions. In other words, for these two operating points, the flow is time-periodic in the frame of reference of each row. After reaching the unsteady periodic state, a full rotation of the rotor is performed to extract data (unsteady and time averaged). The time-averaging period is equal to one rotor rotation. For the OP3 operating point, an unsteady vortex shedding phenomenon emerged at a frequency well below the blade passing frequency. This phenomenon is detailed in Ref. [20]. The simulation of such unsteady phenomenon has been possible thanks to the extension of the calculation domain to the complete circumference. For this case, after reaching the stable state, the simulation has been extended during six rotor rotations to validate the stability of the operating point and to extract data. The time-averaging period is therefore equal to six rotor rotations. Considering the stall transient simulation, nine physical rotor rotations have been simulated after modifying the throttle condition. Because of the domain size, the data extraction of the complete flow field is hardly affordable with a correct temporal resolution. Therefore, data extraction is segregated into local information recorded at each time step (numerical probe), two-dimensional planes extracted every ten time steps (blade-to-blade and cross stream), and the complete three-dimensional field saved three times per impeller rotation.

4 Validation of the Numerical Model

The characteristic curve of the compressor stage from the unsteady simulations and from the experimental measurements is represented in Fig. 3. All these operating points are stable. It depicts the total-to-static pressure ratio defined as $\pi = p_{s4}/p_{t1}$ as a function of the corrected mass flow. The corrected mass flow is defined as

$$\dot{m}_{cor} = \frac{\dot{m}\sqrt{T_{t1}/T_{ref}}}{p_{t1}/p_{ref}} \qquad (2)$$

The experimental value of p_4 corresponds to the mean value of three static pressure probes located on the hub surface, each 120 deg, at diffuser exit radius. The static pressure from the numerical results is time averaged and extracted at the same locations. Concerning the global performances, the three computed operating points are in good agreement with the experimental data.

5 Flow Pattern Evolution Along the Speed Line

The present part presents the main evolutions of the flow structure developing in the impeller and in the vaned diffuser when the mass flow is reduced from the operating point OP1 (peak efficiency) to the operating point OP3 (operating point localized on the positive slope). Investigations focus on the inlet of the component where the effect of the rise of the incidence is the largest.

5.1 Flow Features in the Impeller. The mass flow reduction from the operating point OP1 to OP3 leads to the emergence of an unsteady mechanism that comes from the rise of the incidence angle on the impeller blades. An increase in the mean incidence angle from 4 deg to 12 deg is observed, which initiates a separation of the boundary layer on the impeller blade suction side. The boundary layer separation is present all over the span. Figure 4 represents the line integral convolution of the skin-friction pattern on the impeller blade suction side, for the operating points OP1 and OP3. For the sake of clarity, only 70% of the meridional coordinate is represented. The boundary layer separates at the leading edge and reattaches further downstream (white dashed line). Also, the incidence angle increases from hub to shroud. This is why the separation zone is larger near the shroud than near the hub. It can also be noticed that the friction lines in the separation zone are oriented toward the radial direction. It means that the low momentum fluid initially in the boundary layer is driven toward the
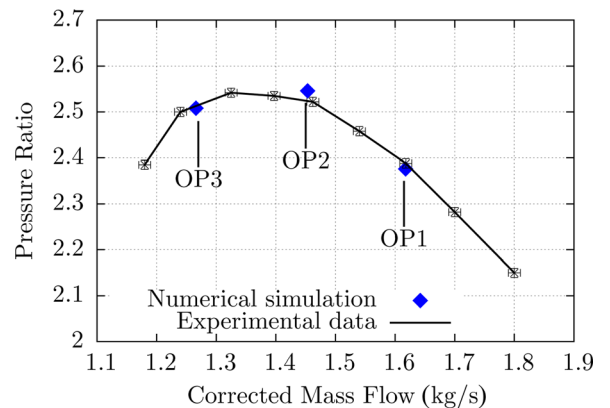

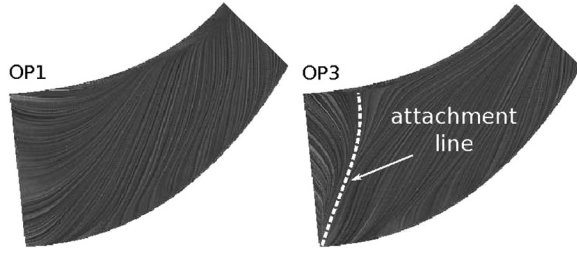Fig. 3 Pressure ratio of the compressor stage

Fig. 4 Line integral convolution of the skin-friction pattern on the impeller blade suction side

Fig. 6 Isosurface of positive axial velocity (blue), isosurface of negative axial velocity (red), and isosurface of λ_2 vortex criteria (golden) for the operating point OP3

shroud. At the tip of the blade, this low momentum flow interacts with the leakage flow. It is transported and stretched all over the circumferential direction. As a result, the flow structure for the operating point OP3 is marked by an accumulation of low momentum fluid near the shroud between the suction side of the main blade and the pressure side of the splitter blade. This mechanism and the low momentum flow region are presented in Fig. 5, which shows the time-averaged meridional velocity in section B (see also Fig. 2). Due to velocity difference, the interface between the main flow (high-speed fluid) and this low momentum flow forms an intense shear layer. The intensity of the shear layer in terms of vorticity magnitude is such that a Kelvin–Helmholtz instability develops and generates a periodic vortex shedding. Figure 6 [21] represents an isosurface of the λ_2 vortex criteria (golden), an isosurface of positive axial velocity (blue) representing the main flow, and an isosurface of negative axial velocity (red) representing the low momentum flow.

The objective of the λ_2 vortex criteria is to detect the vortex cores. To do so, the velocity gradient tensor **J** is decomposed into its symmetric part **S** and antisymmetric part Ω, and the eigenvalues of $\mathbf{J}^2 + \Omega^2$ are determined. If the second eigenvalue λ_2 is negative in a region, it belongs to a vortex core. In Fig. 2, it can be noticed that the vortex is localized at the interface between the two flow structures, and that it extends from 80% span to the shroud.

This vortex shedding phenomenon is observed identically in every blade passage. Six vortices per blade passage are shed during one physical impeller rotation. Therefore, in the rotating frame, this unsteady mechanism leads to the emergence of a reduced frequency $f^* = f/f_R = 6$ in the frequency spectrum. It also induces losses in the impeller, which contribute to reduce the pressure ratio of the stage when the operating point moves from OP2 to OP3. The slope of the characteristic curve is then positive (see again Fig. 3).

5.2 Flow Features in the Diffuser. The flow topology in the vaned diffuser is also significantly modified by the mass flow
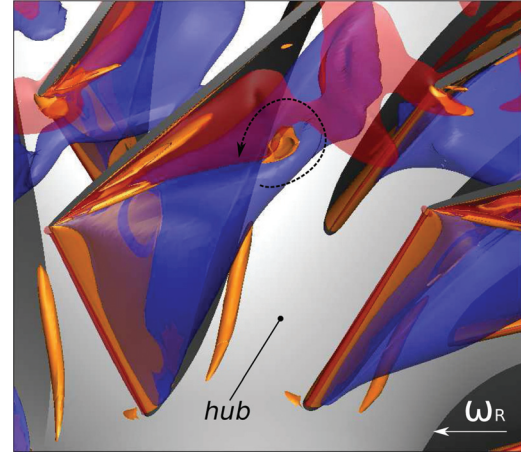
reduction. These modifications are also related to the excess of the incidence angle. When the mass flow is reduced, the mean tangential velocity at the impeller exit increases (due to impeller backswept angle) due to the reduction of the mean radial velocity. This causes an increase in the absolute flow angle all over the span. In addition, the flow at the impeller exit is highly distorted in the spanwise direction due to the meridional curvature and the leakage flows that develop in the impeller. They induce a reduction of the meridional velocity near the shroud and cause a significant rise of the absolute flow angle. Figure 7 represents the axisymmetric time-averaged incidence angle for the three operating points on the diffuser vane, from hub to shroud. The natural increase in the incidence due to the mass flow reduction is clearly observable. Besides this effect, the large increase of the incidence from 80% of the span to the shroud is also observed for the three distributions. As mentioned previously, this rise of incidence is induced by the leakage and secondary flows which concentrate in the upper half of the span. For the operating point OP3, the excessive positive incidence angle near the shroud triggers the separation of the boundary layer on the suction side near the leading edge of the diffuser vane. Figure 8 illustrates the separation by representing the time-averaged streamlines and the radial velocity contour at 90% span, at the diffuser inlet. The red zone shows negative radial velocity (reverse flow) while the blue zone shows positive radial velocity. The three-dimensional topology of the separation region has also been investigated with an instantaneous isosurface of the λ_2 vortex criteria (Fig. 8). The isosurface is colored by the normalized span. It illustrates a vortex core extending from the diffuser
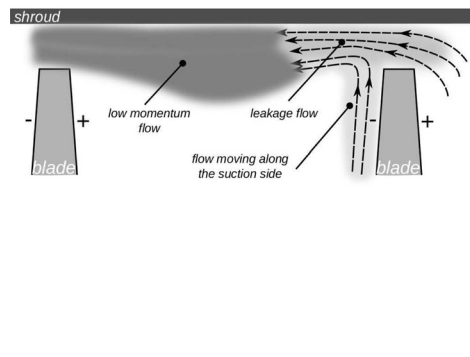

Fig. 5 Illustration of flow mechanism in the blade tip region (left) and contour of time-averaged reduced meridional velocity at section B for OP3 operating point (right)
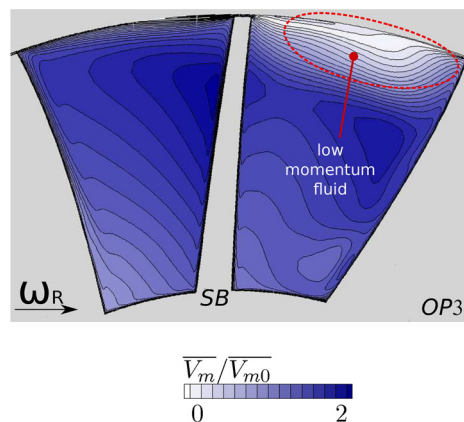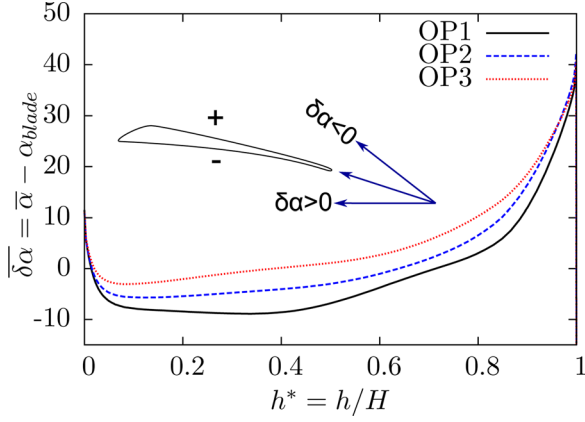
Fig. 7 Time-averaged axisymmetric profile of the incidence angle at the diffuser inlet from hub ($h^* = 0$) to shroud ($h^* = 1$)
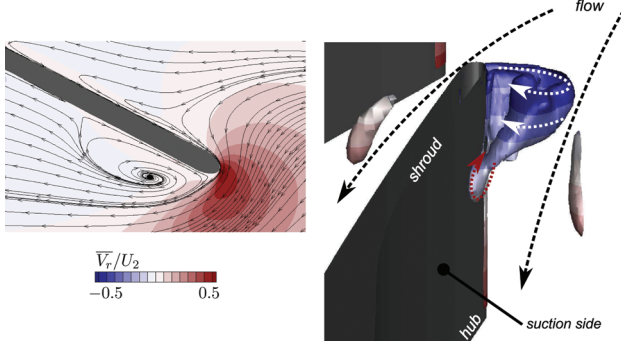

Fig. 8 Contour of time-averaged reduced radial velocity at 90% span at the diffuser inlet (left) and isosurface of the λ_2 vortex criteria (right) for the operating point OP3

vane suction side (60% span) to the shroud. The gradual increase in the incidence angle near the shroud makes the upper end of the vortex tube divert from the diffuser vane suction side. Such topology has already been observed recently by Everitt and Spakovszky [22] in the radial diffuser of a centrifugal compressor stage. They observed that the excess of incidence angle near the shroud leads to a boundary layer separation on the suction side. They also demonstrate that the association of the boundary layer separation with the negative radial velocity allows the vorticity in the separated region to be shed in the vaneless space and to travel circumferentially. The accumulation of vortical structures in the vaneless space forms the spike disturbance, which finally leads to the destabilization of the flow in the vaned diffuser. In the present case, unsteady analysis has revealed that the vortices appear on the suction side, grow in size, detach from the suction side, and finally get convected downstream toward the diffuser outlet. Therefore, the accumulation of vortical structure in the vaneless space is not observed here, explaining why the flow in the diffuser is still stable for the operating point OP3.

5.3 Modal Analysis in the Vaneless Space. In centrifugal compressor stages, the interaction between the impeller and the vaned diffuser induces circumferential spatial modes. As mentioned in the introduction, stall onset can be triggered by the development of a modal wave. For these reasons, the modal content has been analyzed following the Tyler and Sofrin model [23]. This model states that the flow can be decomposed into a superimposition of circumferential spinning modes. The mode order m_θ is expressed as a linear combination of the numbers of blades of the rotor N_R and of the stator N_S

$$m_\theta = n \cdot N_R + k \cdot N_S, (n,k) \in (Z,Z) \tag{3}$$

For each spatial spinning mode m_θ, the rotation speed is given by

$$\omega_{m_\theta} = \frac{n \cdot N_R}{m_\theta} \cdot \omega_R \tag{4}$$

Hence, the circumferential modes are identified through the determination of two integers n and k. The modal decomposition is performed by first extracting static pressure signals all over the circumferential position for each time step $p(\theta, t)$, for a given axial and radial position. The extraction is performed over 360 deg at a frequency of 168 samples for a single impeller rotation. Second, a circumferential average is carried out on each signal to obtain the term referenced as $\overline{p(t)}^\theta$, representing the instantaneous mean axisymmetric value. The spatial fluctuation is then determined as follows:

$$\widetilde{p(\theta,t)} = \frac{p(\theta,t) - \overline{p(t)}^\theta}{\overline{p(t)}^\theta} \tag{5}$$

Finally, a spatial Fourier transform is applied at each time step to build the complex function $P(m_\theta, t)$ that describes the temporal evolution of the spatial modes m_θ. The amplitude of the modes corresponds to the absolute value of the complex function $P(m_\theta, t)$. The temporal evolution of the phase of the complex function $P(m_\theta, t)$ is also an interesting information. It allows to determine the correct combination (n, k). Indeed, for a given spatial mode m_θ, several set of (n, k) are possible. For example, in the study case containing an impeller with eight blades and a diffuser containing 21 vanes, the spatial mode 17 can be obtain with the formulation $(-11 \cdot N_R + 5 \cdot N_S)$ or with the formulation $(10 \cdot N_R - 3 \cdot N_S)$. The temporal evolution of the phase permits to know the correct couple (n, k) by observing the number of cycles of the phase during a single impeller rotation.

This frequency treatment is applied at the shroud in the vaneless space during a single rotation. Figure 9 represents the temporal evolution of the amplitude of the first 30 spatial modes for the operating points OP1 and OP3. For the operating point OP1, as it
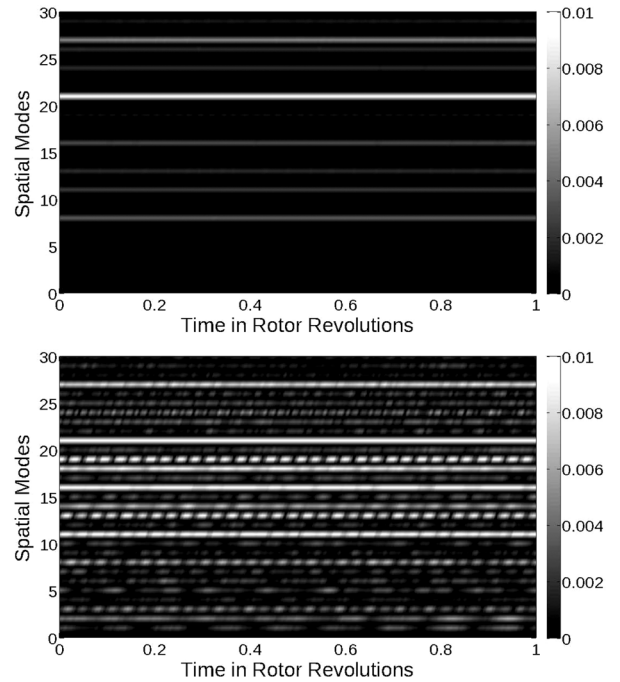

Fig. 9 Amplitude of the spatial modes for the operating point OP1 (top) and for the operating point OP3 (bottom)

is expected, the spatial modes $m_\theta = n \cdot N_R = n \cdot 8$ induced by the impeller blade and the spatial modes $m_\theta = k \cdot N_S = k \cdot 21$ induced by the diffuser vanes are noticeable with the largest levels of amplitude. The modes $m_\theta = 11$, $m_\theta = 13$, and $m_\theta = 27$ have also a high amplitude value. For these three modes, the phase leads to the identification of the associated rotation speed which is, respectively, equal to $2.9\omega_R$, $-0.61\omega_R$, and $1.77\omega_R$. These rotation speeds corroborate the Tyler and Sofrin model by taking the couples $m_\theta = 4 \cdot NR - 1 \cdot N_S$, $m_\theta = -1 \cdot NR + 1 \cdot N_S$, and $m_\theta = 6 \cdot NR - 1 \cdot N_S$. Then, the origin of these spatial modes comes from the interaction between the impeller and the vaned diffuser. When the mass flow is reduced to the operating point OP3, the modal content significantly expands. The amplitude of the spatial mode rises for the majority of them. However, the main particularity concerns low-order modes ($m_\theta < 5$). Indeed, while the high-order modes ($m_\theta > 5$) come from the interaction mechanisms, the low-order modes do not follow the Tyler and Sofrin model and do not take their origins from the interaction between the rows. They could be linked to the operation of the compressor on the positive slope and to resonance phenomena of the compression system. In addition to the emergence of low-order modes at near stall conditions, it can be observed that the amplitude of the spatial modes fluctuates in time while it is almost constant for the operating points OP1. The mode induces circumferential distortions of the flow quantities such as incidence on the blade. Then, the rise of the amplitude of the modes may lead to local separation on the blade and to the possible appearance of spike [6].

6 Investigation of the Stall Onset Mechanisms

6.1 Global Performance. The method used to simulate the stall inception mechanisms consisted in modifying slightly the throttle parameter until a large drop in mass flow rate is observed. The closing step ($\delta\lambda$) of the throttle has been minimized in order to avoid influence on the natural development of the mechanism. To do so, from the stable operating point OP3, the throttle parameter is increased step-by-step. For each step, the simulation is run to complete three impeller rotations. If the stall inception does not occur during these three rotations, the throttle is closed again. This methodology has permitted to know the throttle parameter for which the compressor is unstable. This throttle value is named (λ_{stall}). The throttle parameter for the last stable operating point is defined as $\lambda_{limit} = \lambda_{stall} - \delta\lambda$. The increase in static pressure generated by the increase in the throttle parameter is less than 0.1% of the initial mean value. Figure 10 represents the mass flow at the inlet and at the outlet of the numerical domain during nine impeller rotations at the throttle condition λ_{limit}, followed by nine impeller rotations at the throttle condition λ_{stall}. From $t = 0$ rev,

Fig. 10 shows that the mass flow slightly decreases during the first two rotations. Between the second and fourth rotations, the mass flow reduction is larger to finally drop from $t = 4$ rev until the end of the simulation. The simulation is stopped after nine impeller rotations as the mass flow rate has reached a reduction of 40% of the initial value. As shown by Emmons et al. [12], the drop in pressure ratio may be abrupt or progressive. Figure 11 represents the pressure ratio of the stage during the stall transient. It can be noted that the drop in pressure ratio is progressive.

6.2 Emergence of the First Spatial Mode. As mentioned in the Introduction, studies related to investigations of stall inception mechanisms have mainly be performed through experimental procedures. Generally, unsteady pressure measurements are performed thanks to high-frequency response pressure transducers located at casing all over the circumferential extent. In the present study, a similar procedure has been reproduced and signals are obtained from seven numerical probes distributed circumferentially on the shroud and at the inlet of the diffuser. The probes record the conservative variables at each time step and permit to calculate afterward all the aerodynamic quantities. Figures 12 depicts the static pressure from $t = -2$ rev to $t = 9$ rev. To remove the trace of the impeller blade passing, the signals have been time averaged by using a central moving average over a window length equal to the blade passing period. The aim of this operation is to filter the effect of the blade passing to improve the detection of the emergence of a new unsteady phenomenon. The static pressure signals show the development of a modal wave rotating in the direction of the impeller rotation. The rotation speed of the modal wave is equal to approximately 50% of the impeller speed.

Fig. 11 Evolution of the total-to-static pressure ratio during the stall onset. The throttle condition is modified at $t = 0$ rev.
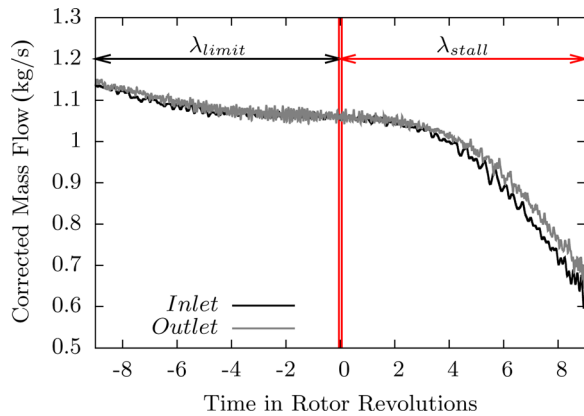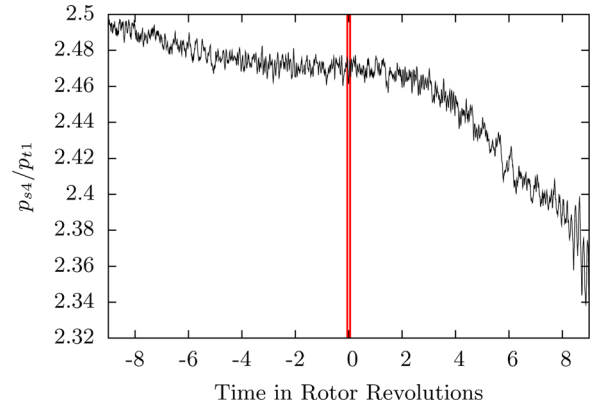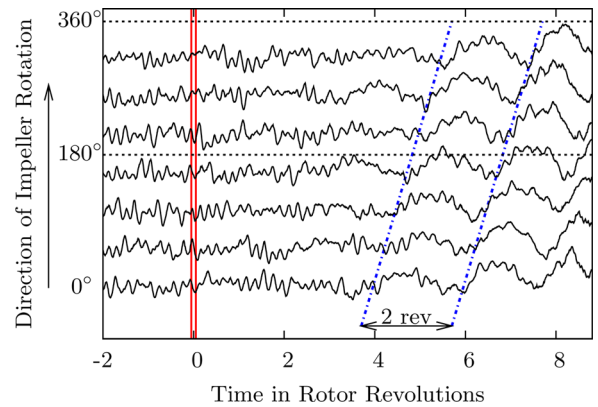

Fig. 10 Evolution of the mass flow at the inlet and at the outlet of the calculation domain during the stall onset simulation. The throttle condition is modified at $t = 0$ rev.

Fig. 12 Pressure signals during the stall onset extracted at shroud in the vaneless space. The throttle condition is modified at $t = 0$ rev.
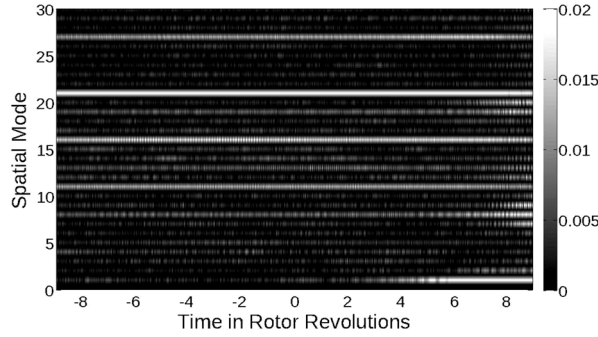
Fig. 13 Amplitude of the spatial mode extracted in the vaneless space at shroud. The throttle condition is modified at $t = 0$ rev.
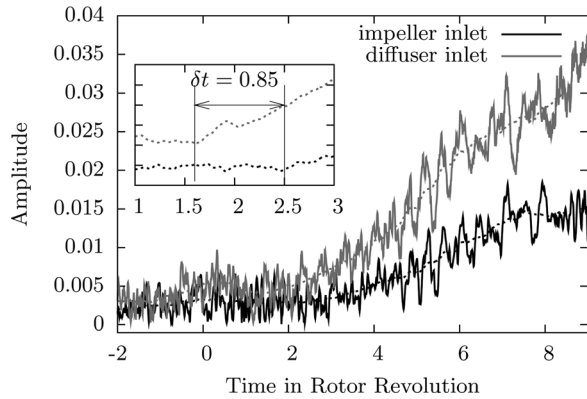

Fig. 14 Amplitude of the spatial mode $m_\theta = 1$. The throttle condition is modified at $t = 0$ rev.

The length of the modal wave covers the full annulus. It can also be noticed that the amplitude of the modal wave increases until the end of the simulation.

During the simulation of the stall transient, conservative quantities are also extracted all over the shroud surface of the stage (impeller and diffuser). Then, the static pressure can be extracted in the vaneless space all over the circumferential position at the casing to conduct the modal analysis presented in Sec. 5.3. Figure 13 represents the evolution of the amplitude of the first 30 spatial modes m_θ from $t = -9$ rev to $t = 9$ rev. As expected, the spatial mode $m_\theta = 2 \cdot N_R = 2 \cdot 8$ induced by the impeller blades and the spatial mode $m_\theta = N_S = 21$ induced by the diffuser vane have the largest amplitudes. The spatial modes $m_\theta = 11$ and $m_\theta = 27$ have also large amplitudes. As discussed previously, they come from the interaction between the rotor and the stator. However, the main particularity concerns the evolution of the amplitude of the first spatial mode $m_\theta = 1$. The characteristic of this mode does not follow the Tyler and Sofrin formulation. It does not take its origin from the rotor–stator interaction. To further investigate the origin of this mode, the modal analysis is extended to static pressure data set extracted at the impeller inlet. More precisely, the extraction of the static pressure over the circumferential coordinate is performed at the shroud, 5 mm upstream the impeller leading edge. Figure 14 represents the amplitude of the first mode ($m_\theta = 1$) extracted at the impeller inlet and in the vaneless space from $t = -2$ rev to $t = 9$ rev. It shows that the increase in the amplitude occurs first in the vaneless space and approximately at $t = 1.65$ rev. Then, the emergence of the mode occurs in the vaneless space and propagates upstream and downstream in the compressor stage. Therefore, there is a time lag ($t_l \approx 0.85$ rev) between the detection of the rise of the amplitude of the mode in the vaneless space and at the impeller inlet. The propagation of the modal wave up to the impeller inlet is a characteristic of this compressor as the flow is subsonic. In transonic compressors, the work of Trebinjac et al. [24] shows that unsteadiness in the vaneless space was not detected at the impeller inlet. The evolution of the amplitude of the first mode has also been extracted at 10%, 50%, and 90% of the span (not represented here) in the vaneless space. It has been observed that the evolution of the amplitude is identical whatever the span is. The fact that the modal wave propagates upstream means that it interacts with the impeller flow structure. Section 6.3 of the paper focusses on this interaction.

6.3 Effect of the Mode Emergence on the Flow Structure.
The effects of the evolution of the first spatial mode are now presented. To do so, investigations were performed at $t = -2$ rev and all over the development of the modal wave. At $t = -2$ rev, the throttle has not been closed yet. It can be considered that at this instant, the compressor operates near the limit of stability as further throttling leads to the stall onset. The flow topology at this instant is slightly different compared with the one described previously for the operating point OP3. In fact, as the mass flow is lower, the unsteady mechanism leading to the vortex formation is more intense (incidence is larger). Figure 15 represents a contour of static pressure at the blade tip (98% span) and two isosurfaces of density at the impeller inlet. The presence of the vortex can be tracked by the rounded low-pressure region that it induces. The trajectory of the vortices is represented by the arrow. It can be noticed that the vortices trajectory is highly tangential, and that they are now convected in the right midchannel (channel composed of main blade pressure side and the splitter blade suction side). The isosurfaces of density give a three-dimensional representation of the vortex tube. It can be seen that the vortex spans from the suction side of the main blade to the shroud. Such vortices structures have been observed recently by Pullan et al. [7] on an axial configuration. They form the starting point of the spike-type disturbance which leads to stall inception. However, in the
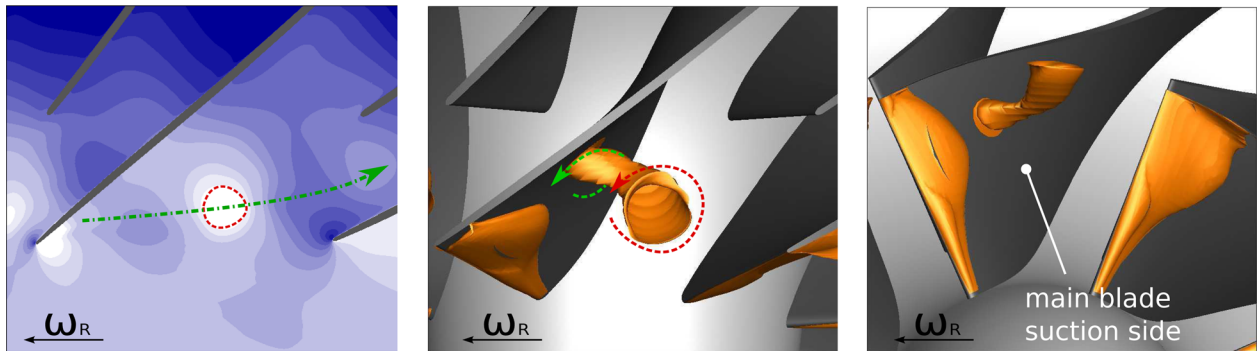

Fig. 15 Contour of instantaneous static pressure at 98% span at $t = -2$ rev (left); isosurface of instantaneous density at $t = -2$ rev (middle and right)
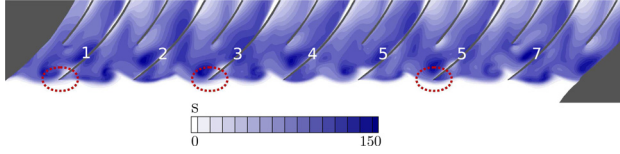
Fig. 16 Contour of instantaneous entropy at 98% span at $t = -2$ rev

Fig. 18 Pressure signals during the stall onset extracted at the shroud at the impeller inlet. The throttle condition is modified at $t = 0$ rev.

present case, no spike disturbance has been observed at the impeller inlet.

Another important characteristic concerns the position of the interface between the leakage flow and the main flow. In axial configurations, Vo et al. [25] mentioned that there are two conditions for the formation of spike disturbance in axial configuration. The first one is the alignment of the interface between the main flow and the leakage flow with the leading edge plane. The second one concerns the presence of a backflow region at the trailing edge. This second criterion has no real sense in centrifugal configuration. However, the first criterion is satisfied as it can be see in Fig. 16 representing an instantaneous contour of entropy at the blade tip for the height channels. Depending on the position of the vortex in the channels, the leakage flow of a blade reaches the leading edge of the adjacent blade. This is the case for the blades 1, 3, and 6 (red circles) at the instant $t = -2$ rev. This criterion is therefore relevant for this configuration and could be used as an indicator of stall. However, such observation needs to be generalized to other centrifugal compressors.

The flow topology present at $t = -2$ rev is modified by the emergence of the first spatial mode. The mode induces a circumferential distortion of the flow noticeable in the complete stage. It generates an increase in the static pressure on the first-half of the circumference of the compressor and a decrease in the static pressure on the second-half of the circumference (the mode has one lobe). Then, at the impeller inlet, the distortion of the pressure field modifies the trajectory of the vortices. The trajectory becomes more tangential in four adjacent channels while it becomes less tangential in the four others. Thus, when the amplitude of the mode has reached a specific value, vortices come out of the channel and travel upstream of the leading edge of the main blades. The jump of a vortex from one channel to the next occurs first at the instant $t = 4.34$ rev. Figure 17 represents a static pressure contour extracted at the casing and at the impeller inlet for three different times. At the instant $t = 4.19$ rev (bottom), the vortex is in the middle of the channel composed of blades 3 and 4 (red arrow). Some time later ($t = 4.34$ rev), the vortex is in front of the leading edge of the blade 4 to finally travel in the adjacent channel composed of blades 4 and 5. The evolution of this phenomenon is also observable from static pressure signals recorded by eight numerical probes positioned circumferentially at the
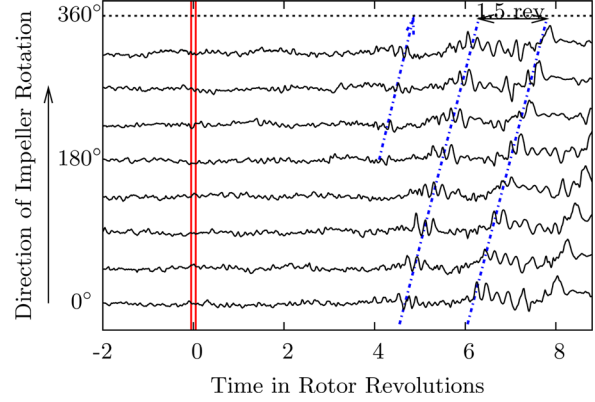
shroud, 1 mm upstream of the leading edge plane. Figure 18 represents the pressure signals for the eight probes after filtering the blade passing frequency. The presence of vortices traveling upstream of the leading edge plane is first tracked by the sensor S5 at the instant $t = 4.1$ rev (see arrow in Fig. 18). It is then successively detected by the sensors S6, S7, S8. In the absolute frame, the vortices rotate in the direction of the impeller rotation but at a lower speed.

As it was demonstrated previously (Fig. 14), the amplitude of the first mode rises continuously with time. Then, the flow distortion becomes more and more important. As a result, the number of vortices traveling upstream the leading edge plane increases. Pressure signals from Fig. 18 show that the disturbance starts with a single low-pressure trace (sensor S5, $t = 4.1$ rev). It means that only one single vortex is traveling upstream. At the instant $t = 4.4$ rev, the disturbance recorded by the sensor S8 shows two low-pressure traces, meaning that the two vortices travel upstream. This mechanism continues to amplify and the number of vortices rotating upstream of the impeller increases. In order to investigate the effect of this mechanism on the impeller performance, Fig. 19 represents the total-to-total pressure ratio of the impeller during the stall transient. It can be observed that when the disturbance starts to develop ($t = 4$ rev sensor S5), the pressure ratio of the impeller stops rising. It is approximately constant from $t = 4$ rev to $t = 6$ rev, to finally decrease after $t = 6$ rev. The constant rise of the amplitude of the first mode generates a continuous drop in impeller pressure ratio. The slope of the compressor characteristic becomes larger than the one of the throttle. It means that the pressure delivered by the compressor is too low to face the pressure imposed by the throttle. This results in a continuous reduction of mass flow.
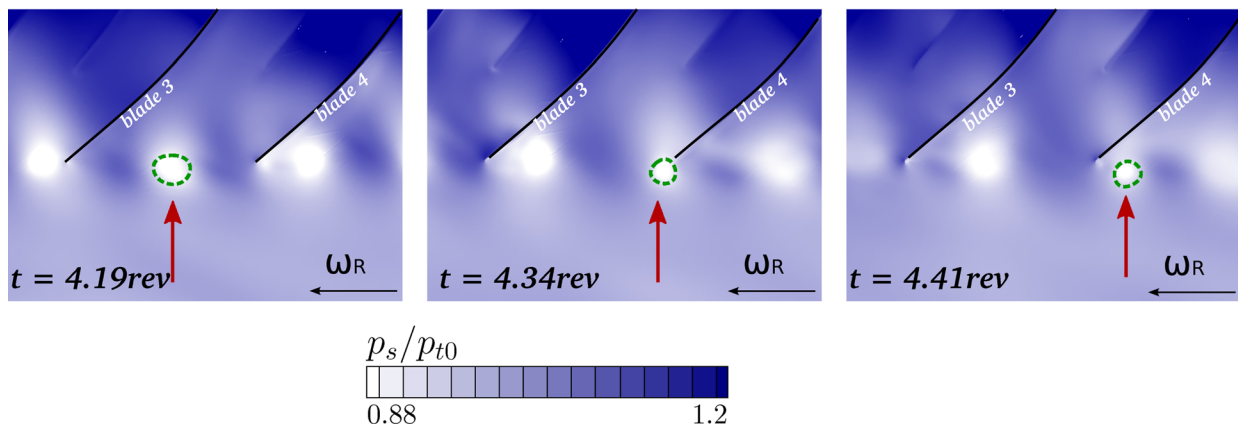

p_s/p_{t0}

0.88   1.2

Fig. 17 Contour of instantaneous static pressure at the shroud and at the impeller inlet
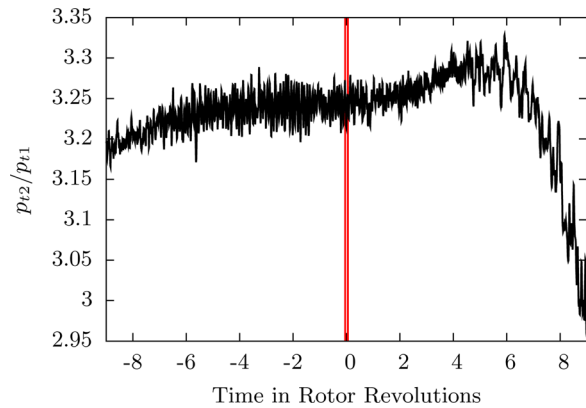
Fig. 19 Evolution of the total-to-total pressure ratio of the impeller during the stall transient. The throttle condition is modified at $t = 0$ rev.

Conclusion

Unsteady simulations have been performed to highlight the stall inception process in a centrifugal compressor stage. The mass flow reduction leads to significant modifications of the flow pattern at the inlet of both components: impeller and diffuser. Boundary layer separates on the suction side and forms a vortex tube that spans from the blade suction side to the casing. Even though this topology is known to be the starting point of spike-type disturbance formation, the trajectory of the vortices is such that no spike disturbance has been observed. However, stall inception mechanisms involve the growth of the amplitude of a modal wave rotating in the vaneless space. As the flow in the compressor is subsonic, the wave propagates upstream and interacts with the impeller flow structure. This interaction leads to the drop in the impeller pressure ratio and inherently the stage pressure ratio. The slope of the compressor characteristic is larger than the one of the throttle, leading to a continuous reduction of the mass flow.

Acknowledgment

Nomenclature

f = frequency (s^{-1})
H = blade height
m_θ = spatial mode
$\dot{m}$ = mass flow (kg/s)
MB, SB = main blade, splitter blade
N = number of blades
p = pressure (Pa)
PS, SS = pressure side, suction side
s = entropy (J/K/kg)
t = time (s)
T = time period (s), temperature (K)
U = impeller speed (m/s)
V = absolute velocity (m/s)

Greek Symbols

α = absolute flow angle (deg)
λ = throttle parameter
ω = rotation speed (rad/s)

Subscripts and Superscripts

cor = corrected
$\bar{f}$ = time-averaged value of f
in = inlet
m, r, t = meridional, radial, and tangential
out = outlet
R = rotor
ref = reference conditions
s = static quantity
S = stator
t = total quantity
0 = location of the calculation domain inlet
1 = location of the impeller inlet
2 = location of the impeller exit
4 = location of the diffuser exit
5 = location of the calculation domain outlet
$*$ = reduced quantity

References

[1] Greitzer, E. M., 1981, "The Stability of Pumping Systems—The 1980 Freeman Scholar Lecture," ASME J. Fluids Eng., **103**(2), pp. 193–242.
[2] Cumpsty, N., 2004, *Compressor Aerodynamics*, Krieger Publishing, Malabar, FL.
[3] Skoch, G. J., 2003, "Experimental Investigation of Centrifugal Compressor Stabilization Techniques," ASME J. Turbomach., **125**(4), pp. 704–713.
[4] McDougall, N. M., Cumpsty, N. M., and Hynes, T. P., 1990, "Stall Inception in Axial Compressors," ASME J. Turbomach., **112**(1), pp. 116–125.
[5] Day, I. J., 1993, "Stall Inception in Axial Flow Compressor," ASME J. Turbomach., **115**(1), pp. 1–9.
[6] Camp, T. R., and Day, I. J., 1998, "1997 Best Paper Award—Turbomachinery Committee: A Study of Spike and Modal Stall Phenomena in a Low-Speed Axial Compressor," ASME J. Turbomach., **120**(3), pp. 393–401.
[7] Pullan, G., Young, A. M., Day, I. J., Greitzer, E. M., and Spakovszky, Z. S., 2015, "Origins and Structure of Spike-Type Rotating Stall," ASME J. Turbomach., **137**(5), p. 051007.
[8] Day, I. J., 2016, "Stall, Surge, and 75 Years of Research," ASME J. Turbomach., **138**(1), p. 011001.
[9] Trébinjac, I., Bulot, N., Ottavy, X., and Buffaz, N., 2011, "Surge Inception in a Transonic Centrifugal Compressor Stage," ASME Paper No. GT2011-45116.
[10] Spakovszky, Z. S., and Roduner, C. H., 2009, "Spike and Modal Stall Inception in an Advanced Turbocharger Centrifugal Compressor," ASME J. Turbomach., **131**(3), pp. 1–9.
[11] Toyama, K., Runstadler, P. W., and Dean, R. C., 1977, "An Experimental Study of Surge in Centrifugal Compressors," ASME J. Fluids Eng., **99**(1), pp. 115–124.
[12] Emmons, H. W., Pearson, C. E., and Grant, H. P., 1955, "Compressor Surge and Stall Propagation," Trans. ASME, **77**(4), pp. 455–469.
[13] Mizuki, S., and Oosawa, Y., 1992, "Unsteady Flow Within Centrifugal Compressor Channels Under Rotating Stall and Surge," ASME J. Turbomach., **114**(2), pp. 312–320.
[14] Cambier, L., and Gazaix, M., 2002, "ElsA: An Efficient Object-Oriented Solution to CFD Complexity," AIAA Paper No. 2002-0108.
[15] Spalart, P. R., and Allmaras, S. R., 1994, "A One-Equation Turbulence Model for Aerodynamic Flows," La Recherche Aérospaciale, **1**, pp. 5–21.
[16] Jameson, A., 1991, "Time Dependent Calculations Using Multigrid, With Applications to Unsteady Flows Airfoils and Wings," AIAA Paper No. 91-1596.
[17] Yoon, S., and Jameson, A., 2002, "An LU-SSOR Scheme for the Euler and Navier–Stokes Equation," AIAA Paper No. 87-0600.
[18] Dufour, G., Carbonneau, X., Arbez, P., and Cazalbou, J. B., 2004, "Mesh-Generation Parameters Influence on Centrifugal-Compressor Simulation for Design Optimization," ASME Paper No. HT-FED2004-56314.
[19] Filola, G., Pape, M. C. L., and Montagnac, M., 2004, "Numerical Simulations Around Wing Control Surfaces," 24th International Congress of the Aeronautical Sciences, Yokohama, Japan, Aug. 29–Sept. 3.
[20] Bousquet, Y., Binder, N., Dufour, G., Carbonneau, X., Roumeas, M., and Trébinjac, I., 2016, "Numerical Investigation of Kelvin-Helmholtz Instability in a Centrifugal Compressor Operating Near Stall," ASME J. Turbomach., **138**(1), p. 071007.
[21] Jeong, J., and Hussain, F., 1995, "On the Identification of a Vortex," J. Fluids Mech., **285**, pp. 69–94.
[22] Everitt, J. N., and Spakovszky, Z. S., 2013, "An Investigation of Stall Inception in Centrifugal Compressor Vaned Diffuser," ASME J. Turbomach., **135**(1), p. 011025.
[23] Tyler, J. M., and Sofrin, T. G., 1962, "Axial Flow Compressor Noise Studies," SAE Technical Paper No. 620532.
[24] Trébinjac, I., Kulisa, P., Bulot, N., and Rochuon, N., 2009, "Effect of Unsteadiness on the Performance of a Transonic Centrifugal Compressor Stage," ASME J. Turbomach., **131**(4), p. 041101.
[25] Vo, H. D., Tan, C. S., and Greitzer, E. M., 2008, "Criteria for Spike Initiated Rotating Stall," ASME J. Turbomach., **130**(1), p. 011023.